Fragmentation-Initiation Threshold for Spheres Impacting at Hypervelocity

Andrew J. Piekutowski

University of Dayton Research Institute, 300 College Park Avenue, Dayton, OH 45469-0182, USA

Abstract

Results of impact tests using aluminum bumper sheets ranging from 0.076-mm- to 4.80-mm-thick and impact velocities ranging from 1.98 to 7.19 km/s were used to determine the fragmentation-initiation threshold for aluminum spheres impacting at hypervelocity. This threshold velocity was expressed as a function of the bumper-thickness-to-projectile-diameter ratio (t/D). Tests using 9.53-mm- and 12.70-mm-diameter, 2017-T4 aluminum spheres indicated that the fragmentation-initiation threshold velocity scaled with t/D ratio. Analysis of radiographs from the tests indicated that the material forming the front structure of the debris cloud was produced by quasi one-dimensional loading of the bumper during the initial phase of the impact process.
© 2003 Elsevier Ltd. All rights reserved.

Keywords: aluminum sphere, aluminum target, bumper sheet, debris cloud, flash radiography, fragmentation, fragmentation initiation, plastic deformation, spallation damage, t/D ratio.

1. Introduction

For the case of a sphere impacting a thin sheet at hypervelocity, the fragmentation-initiation threshold velocity is defined as the impact velocity at which a sphere begins to fragment and to form a rudimentary debris cloud. The threshold velocity for the impact is unique for each combination of impact velocity and bumper-thickness-to-projectile-diameter ratio (t/D). The transition from no fragmentation to fragmentation occurs within a narrow range of impact velocities for each t/D ratio. Fragmentation-initiation threshold velocity data were presented in [1] for tests in which 9.53-mm-diameter, 2017-T4 aluminum spheres impacted thin aluminum sheets at normal incidence and at impact velocities up to 4.67 km/s. This paper combines the results of the older tests with the results of recent tests employing very thin aluminum bumper sheets and 9.53-mm- and 12.7-mm-diameter aluminum spheres at impact velocities just above and below 7 km/s. The results of the tests using the larger diameter spheres indicate that the fragmentation-initiation threshold velocity scales when compared on the basis of t/D ratio. In addition, the recent tests indicate that the relationship used in [1] to describe the fragmentation-initiation threshold velocity is valid for the normal impact of spheres with thin sheets at impact velocities of up to 7.2 km/s. The 7 km/s tests also furnished data that provided insight into the origin of a dark substructure that was previously observed in the front element of several debris clouds.

2. Experimental Procedures

All impact tests were performed in the University of Dayton Research Institute (UDRI) Impact Physics Laboratory using a 50/20 mm, two-stage, light-gas gun. Impact velocities for the tests described in this paper ranged from 1.98 to 7.19 km/s. Impact velocity determinations were made with use of four laser-photodetector systems installed at various locations along the flight path of the projectile. Accuracy of the impact velocity determination was better than ± 0.5 percent.

The tests were performed using 9.53-mm- and 12.70-mm-diameter, 2017-T4 aluminum spheres with nominal masses of 1.275 and 3.000 g, respectively. Various thicknesses of 6061-T6 aluminum sheets were used as bumpers for nine of the tests; 0.076-mm-thick, 1100-H18 aluminum sheets and 0.102-mm-thick, 1350-O aluminum strips were each used for two tests. The thinner 6061-T6 bumpers (t/D ratio less than 0.084) were 10.8 cm square and were securely taped to a 3.18-mm-thick, 15.2-cm-square aluminum frame that had an 8.9-cm-square opening cut in its center. The thicker 6061-T6 bumpers and the 1100-H18 bumpers were 15.2 cm square and were held at the corners by screws passing through the sheets into appropriate support posts. The 1350-O aluminum bumpers were 2.54-cm-wide strips that were suspended from a bar mounted in the target chamber and had a small weight attached to the lower end of the strip. All bumpers were installed and impacted normal to the range center line. The atmosphere in the target chamber at the time of impact was air at a pressure of 5 to 9-mm-Hg.

One, two, or three pairs of flash x-rays were used to observe the post impact behavior of the projectile. Field Emission Model 2772, 180 kV dual pulsers and Scandiflash 150 kV remote tubeheads (Model XT 150) with soft x-ray adapters and 1-mm-diameter sources were used to produce the radiographs. The x-ray heads were accurately positioned on the target chamber to provide simultaneous orthogonal views of the debris clouds. The radiographs were also used to determine the displacement and velocity of selected points in the debris clouds. Foam blocks and rags were used, in five of the tests, to "soft catch" the projectiles after they had impacted the bumper sheets. The condition and shape of the recovered spheres were compared with the appropriate radiographs to verify that the analysis of the radiographs was accurate and that the fragmentation-initiation velocity threshold velocity had or had not been exceeded for each of the five tests.

3. Results and Discussion

Failure and fragmentation of a sphere initiated by a hypervelocity impact with a thin sheet is an orderly process. When impact velocities were below the threshold for the initiation of fragmentation, plastic deformation of the front (impacting) surface and the development of a spall failure inside the rear surface of the sphere were the first manifestations of the failure of the sphere. With a slight increase in the impact velocity, the thin shell spalled from the rear of the sphere will tear open and form petals or fragments that may or may not separate from the rear of the sphere. Increasing the impact velocity by 0.5 km/s or less above this transition point results in the formation of a well-developed debris cloud with the various elements described in Ref. 1.

The spall failure developed inside the rear surface of the sphere was reasonably evident in the radiographs from a number of the tests at the higher velocities, but was very difficult to reproduce in photographic prints made from the radiographs. An illustration presented at the left of Fig. 1 describes the various features observed in the radiographs. These same features are evident in the micrograph of the sphere recovered from Shot 4-1722 and shown at the right in Fig. 1. Also evident in the micrograph, but not the radiographs, is a more extensive system of cracks and voids in the rearmost interior portion of the sphere. When the t/D ratio was greater than 0.13, the formation of cracks and swelling of the rear surface of the spheres was the first evidence of failure of the sphere. For tests with the higher t/D ratios, the onset of cracking or swelling was used to define the failure-threshold velocity.
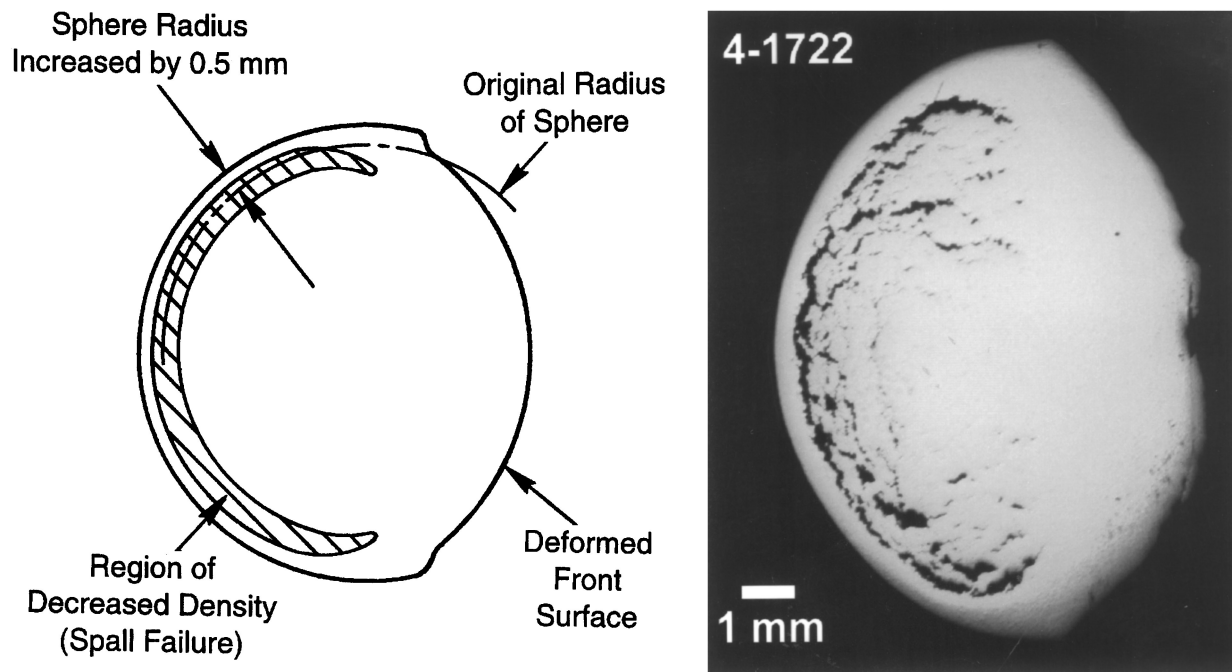
Fig. 1. Illustration taken from the radiograph of a 9.53-mm-diameter aluminum sphere after impact with a 0.465-mm-thick aluminum sheet at 3.37 km/s (Shot 4-1428), showing its plastic deformation and the spall failure at the rear of the sphere. Micrograph is of a 9.53-mm-diameter, 2017-T4 aluminum sphere that struck a 1.257-mm-thick, 6061-T6 aluminum sheet at 2.54 km/s (Shot 4-1722).

Table 1 presents conditions for 13 tests near the threshold velocity and a description of the post impact condition of the sphere. Late-time-view radiographs of the projectiles used for selected tests listed in Table 1 are shown in Fig. 2. Also shown in Fig. 2 are the photographs of the rear surfaces of four of the recovered projectiles. The determination of the post impact condition of the sphere was made with use of the radiographs from each test and, for the lower impact velocities, from an examination of the recovered projectiles.

Table 1. Fragmentation-initiation threshold impact velocity data

| Shot Number	Bumper Sheet Alloy	Sphere Diameter, (mm)	$\frac{t}{D}$	Impact Velocity, (km/s)	Data Source	Post Impact Condition of Rear of Sphere
4-1910	1100-H18	9.53	0.008	7.19	X rays	Attached spall shell
4-1897	1100-H18	9.53	0.008	6.97	X rays	Attached spall shell
4-1870	1350-O	12.70	0.008	6.63	X rays	Attached spall shell
4-1874	1350-O	12.70	0.008	6.41	X rays	Attached spall shell
4-1715	6061-T6	9.53	0.026	4.67	X rays	Attached spall shell
4-1428	6061-T6	9.53	0.049	3.37	X rays	Attached spall shell
4-1633	6061-T6	9.53	0.062	3.65	X rays	Spall shell petalled open, no material lost
4-1632	6061-T6	9.53	0.084	3.47	X rays	Spall shell petalled open, petals detached
4-1722	6061-T6	9.53	0.132	2.54	X rays, recovered sphere	Attached spall shell
4-1719	6061-T6	9.53	0.233	2.83	X rays, recovered sphere	Rear of sphere spalled away
4-1720	6061-T6	9.53	0.233	2.44	X rays, recovered sphere	Several large cracks
4-1718	6061-T6	9.53	0.233	1.98	X rays, recovered sphere	Smooth, no spall or cracks
4-1721	6061-T6	9.53	0.504	2.23	X rays, recovered sphere	Flattened, several small cracks
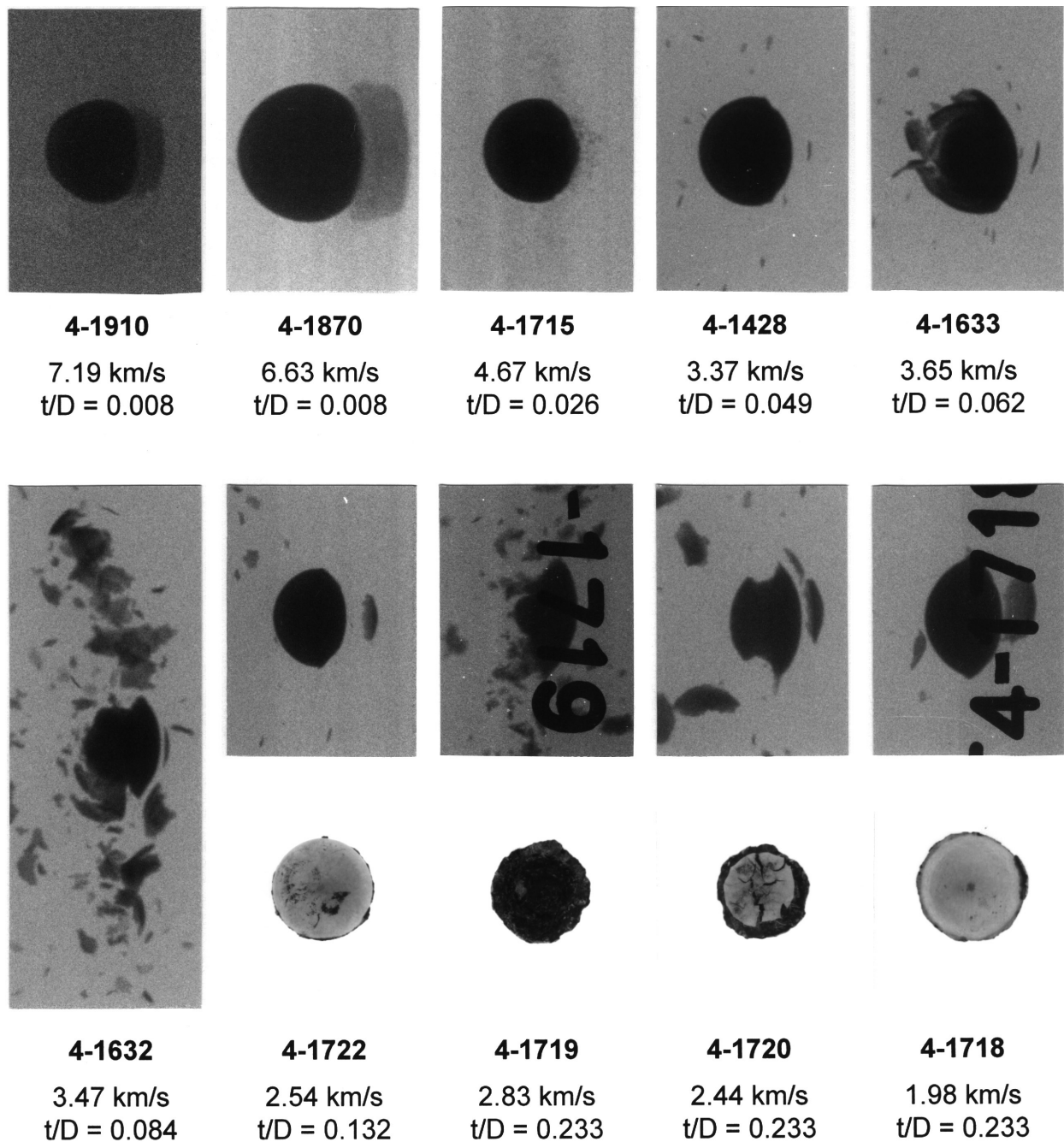
Fig. 2. Late-time-view radiographs and photographs of 9.53-mm- and 12.70-mm-diameter, 2017-T4 aluminum spheres after impact with various thicknesses of aluminum sheets. Spheres are shown traveling from left to right in the radiographs. The rear surfaces of the spheres recovered from foam blocks are shown in the photographs below the appropriate radiographs. Impact conditions for each test are shown below the radiographs/photographs.

The fragmentation-initiation threshold velocity for failure of the sphere is shown as a function of *t/D* ratio in Fig. 3. In Fig. 3, open symbols denote test conditions that produced a separation or a loss of material from the rear surface of the sphere. Solid symbols denote test conditions for which the rear surface of the sphere developed a spall failure but remained intact or was cracked. The equation of the line drawn through the points shown in Fig. 3 was determined from data available at the time of publication of Ref. 1. Data from the four recent tests were simply added to an expanded version of the original figure. The equation giving the threshold velocity, V_S, for failure of the spall shell attached to the rear of the sphere was written as a function of *t/D* ratio as follows:

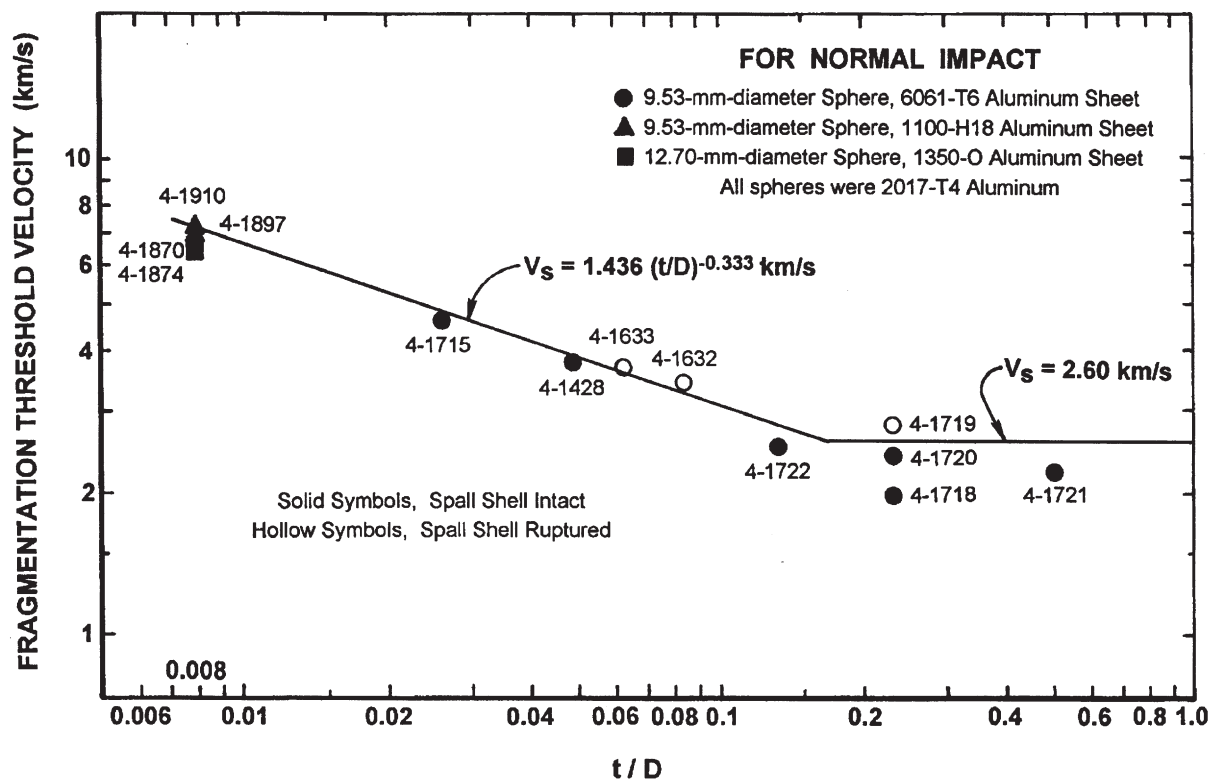$$V_S = 1.436 \, (t/D)^{-0.333} \tag{1}$$

Fig. 3. Fragmentation-initiation threshold velocity as a function of t/D ratio. Shot numbers are shown in this figure to facilitate identification with the data in Table 1 and the radiographs and photographs shown in Fig. 2.

Shot 4-1428 (attached spall shell) and Shot 4-1633 (detached spall shell) provide a reasonably hard "point" through which the line should pass. Exponents ranging from -0.3 to -0.4 would fit a line describing the original data presented in Fig. 3. A value of -0.333 was arbitrarily selected, however, because Gilath *et al.* [2] had shown that the energy required to produce spall-threshold conditions in aluminum was a cubic function of sheet thickness for hemispherical shock waves, a situation similar to the propagation of shocks in the aluminum spheres.

The equation of the line shown in Fig. 3 applies for t/D ratios less than 0.16. A constant threshold velocity of 2.6 km/s was assumed for t/D ratios greater than 0.16. This assumption was based on the observed behavior (see Ref. 1) of the expansion velocity of the shell of spall fragments. When impact velocity was held constant and the t/D ratio was increased, the radial expansion velocity of the shell of spall fragments approached a maximum value when the t/D ratio reached 0.16 to 0.17. The expansion velocity remained relatively constant when the t/D ratio was greater than 0.17. When the t/D ratio was greater than 0.17, an evaluation of the transit times of the shock and release waves in the projectile indicated that the shock would arrive at the rear surface of the sphere relatively unaffected by the release wave originating at the free surface of the bumper. Release waves originating in thinner bumpers, on the other hand, could easily overtake the shock moving toward the rear of the sphere, thereby decreasing the intensity of the shock and the velocity of spall fragments produced when stresses in that region were relieved.

Fragmentation-initiation threshold velocity data were originally available for tests that used 9.53-mm-diameter, 2017-T4 aluminum spheres and impact velocities below 4.67 km/s. However, the recent tests used very thin bumper sheets, 9.53-mm- and 12.70-mm-diameter, 2017-T4 aluminum spheres, and impact velocities that ranged from 6.41 to 7.19 km/s. The results of these newer tests "fit" very nicely on the original plot. Evaluation of the equation for threshold velocity for a test using a t/D ratio of 0.008 indicates that the sphere should fail when the impact velocity is 7.17 km/s. Examination of the radiographs from the recent tests indicated that all four spheres did not fragment but did exhibit a spall failure at their rear surface.

The spall failures observed in the spheres used for the tests with the very thin bumpers were qualitatively the same as those observed in the spheres for the tests using considerably thicker

bumper sheets, with one exception. The spall failures observed for the recent tests did not extend as far around the rear of the sphere as was shown in Fig. 1, but appeared to be confined to an arc that was about 90 degrees in radial extent. In the four new tests, the bulging and separation of the spall shell from the rear of the sphere increased as the impact velocity increased. Note, in Fig. 2, that the rear of the sphere from Shot 4-1910 is considerably more distorted that the rear of the sphere from Shot 4-1870. Although not shown, the separation for Shot 4-1897 was less than that observed for Shot 4-1910 but more than was observed for Shot 4-1870. The separation for Shot 4-1874 was the least observed in the four tests. The material in the spall shell for Shot 4-1910 is under considerable strain. Repeating Shot 4-1910 with a slight higher (about 0.1 km/s) impact velocity would likely result in the spall shell bursting open and, perhaps, releasing one or more fragments. The relationship for threshold velocity that was derived using data from tests at lower impact velocities appears to be viable for impacts up to at least 7.2 km/s.

Comparison of the spall shells from the recent tests and the relationship of the new data to the older data also indicated that the threshold velocity and morphologic features of the debris clouds scaled geometrically when compared on the basis of t/D ratio and impact velocity. Consequently, it is likely that the threshold-velocity relationship given in Fig. 3 would properly describe the onset of failure for spheres of other diameters. Although the failure process for the rear of the sphere appeared to continue unchanged as the impact velocity increased (except for the reduction in the radial extent of the spall failure), the production of a significant front element in the debris cloud was surprising given the minimal thickness of the target sheets.

The observed changes in the properties of the front element of the debris-cloud are noteworthy. In Ref. 1, the front element was shown to develop and grow in an orderly fashion as impact velocity was increased. The development and growth of the front element occurred in the following sequence as the impact velocity increased: a single fragment and/or several solid fragments, a small cloud of solid fragments, and a large cloud of fine droplets of molten aluminum. In general, the front elements were not well-developed unless the impact velocity was reasonably high or, at least, well above the fragmentation-initiation threshold velocity. The radiographs presented in Fig. 2 show the formation of a single large fragment ahead of the deformed sphere for the seven tests at the lower velocities. A small cloud of solid fragments is visible ahead of the deformed sphere for Shot 4-1715. The radiographs from the four recent tests show a front element that appears to be a cloud of very finely divided molten material, e.g., see Shots 4-1870 and 4-1910 in Fig. 2. Not only were the front elements very pronounced (considering the minimal thickness of the bumpers) but they grew in size as they moved downrange.

The essential features of a model for the formation of the front element are shown in the upper right of Fig. 4. The kinematics of the model draw heavily on a description of the impact process given by Ang [3] and used to determine the source of material dominating an impact flash signature. In Fig. 4, U is the shock velocity, u_p is the particle velocity behind the shock, V_0 is the impact velocity, $V_{CP,P}$ is the velocity of the collision point between the surface of the sphere and the target in the reference frame of the projectile, and $V_{CP,T}$ is the velocity of the collision point in the reference frame of the target. $V_{CP,P}$ and $V_{CP,T}$ are given as functions of impact velocity, V_0, sphere radius, R_0, and elapsed time after impact, τ, as follows:

$$V_{CP,P} = \frac{R_0 V_0}{\sqrt{2 R_0 V_0 \tau - V_0^2 \tau^2}} \qquad (2)$$

and

$$V_{CP,T} = \frac{R_0 V_0 - V_0^2 \tau}{\sqrt{2 R_0 V_0 \tau - V_0^2 \tau^2}} \qquad (3)$$
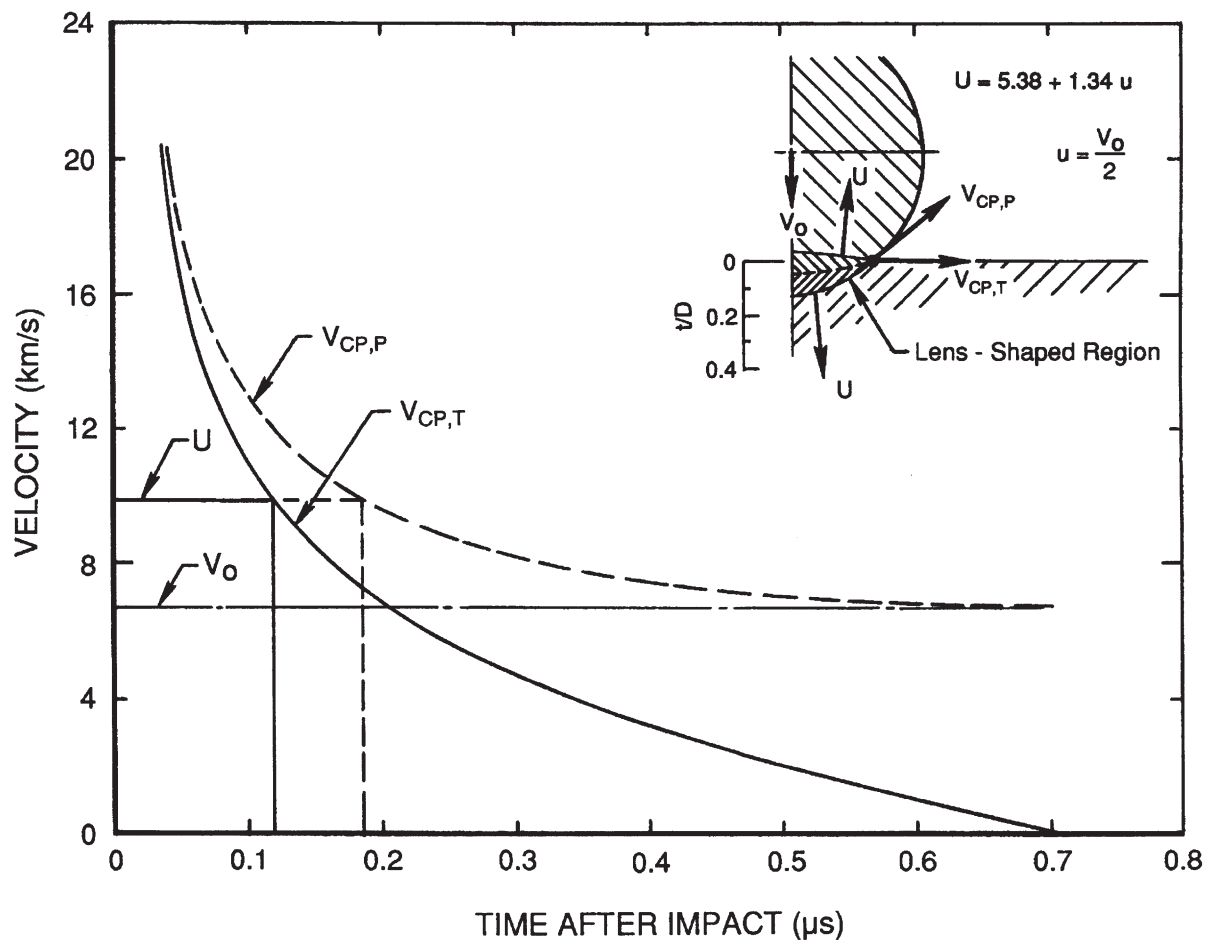
Fig. 4. Illustration of interactions at impact site adapted from work by Ang [3]. Collision-point velocities are shown as a function of time after impact for a 9.53-mm-diameter sphere traveling at 6.70 km/s. In the inset, the impacting sphere and impacted sheet are shown with appropriate notation for the velocities referenced in this paper.

The collision-point velocity, in both frames of reference, is presented in Fig. 4 as a function of time after impact for a 9.53-mm-diameter sphere traveling at 6.70 km/s. Also shown in Fig. 4, as horizontal lines, are V_0 and U. The shock velocity was determined using the relationship given in the upper right of Fig. 4.

As shown in Fig. 4, $V_{CP,T}$ is greater than U for the first 0.12 μs after impact. Consequently, loading of the lens-shaped region shown in the inset was quasi one-dimensional during this time interval. Formation of release waves at the boundaries of the lens-shaped region was not possible as long as $V_{CP,T}$ was greater than U. When $V_{CP,T}$ was less than U, release waves were generated in the target prior to contact by the oncoming sphere. As the impact process continued, formation of release waves in the sphere began and the description of the shock-wave interactions was quickly complicated for the remainder of the impact event. In the inset in Fig. 4, the lens-shaped region of compressed material is shown to scale at the time $V_{CP,T}$ equals U (0.12 μs after impact). The diameter of the compressed region is approximately 56 percent of the diameter of the sphere. Also shown in the inset is a t/D scale that allows the reader to determine the fraction of bumper-sheet thickness that experienced quasi one-dimensional loading during impact.

The growth of a lens-shaped region at the front of an impacting sphere is shown, in Fig. 5, evolving into the dark substructure visible in the front element of the debris cloud shown in the radiograph in this figure. Figure 5 is drawn to scale, although the horizontal axis is compressed. The diameter of the double cross-hatched region in Fig. 5, the dark substructure, was determined from the radiograph. The diameter of this region at 19.8 μs after impact and the measured diametral
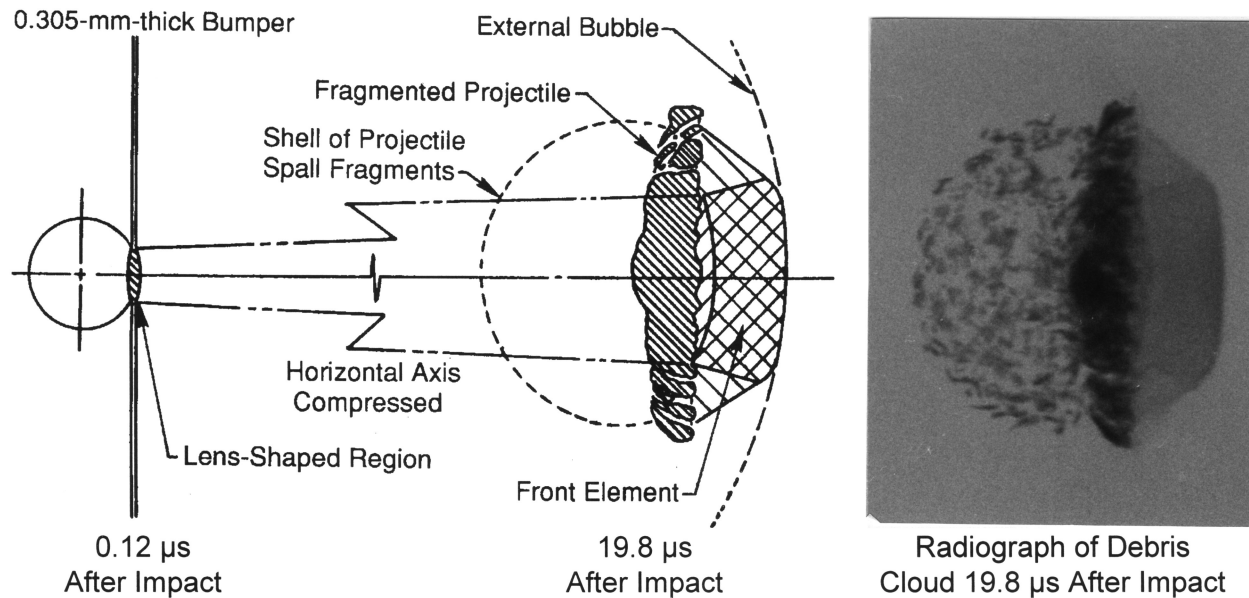
Fig. 5. Development of features in front element of internal structure of debris cloud. View of the debris cloud produced by the impact of a 9.53-mm-diameter, 2017-T4 aluminum sphere with a 0.302-mm-thick, 1100-O aluminum sheet ($t/D = 0.032$) at 6.67 km/s (Shot 4-1290).

velocity of this portion of the debris cloud were used to compute the diameter of the lens-shaped region at 0.12 μs after impact. The nominal diameter of this region was determined to be 56 percent of the sphere diameter, the same percentage determined using the model presented in Fig. 4. An explanation for the formation of the dark substructure in the front element of the debris cloud was not developed in Ref. 1.

Two views of the deformed projectile and the "debris cloud" from Shot 4-1910 are presented in Fig. 6. The radiographs from this test were analyzed to provide displacement and velocity data used to describe the motion and expansion of the front element and the deformed projectile. The results of this analysis are presented in Table 2 with the results of an earlier analysis of selected tests that were described and presented in Ref. 1. The measured velocities presented in Table 2 have been normalized by dividing them by the impact velocity.

The radiographs from Shot 4-1897 show that the front element appears to behave in the same fashion as for Shot 4-1910, but the first view of the debris cloud was made 1.7 μs after impact
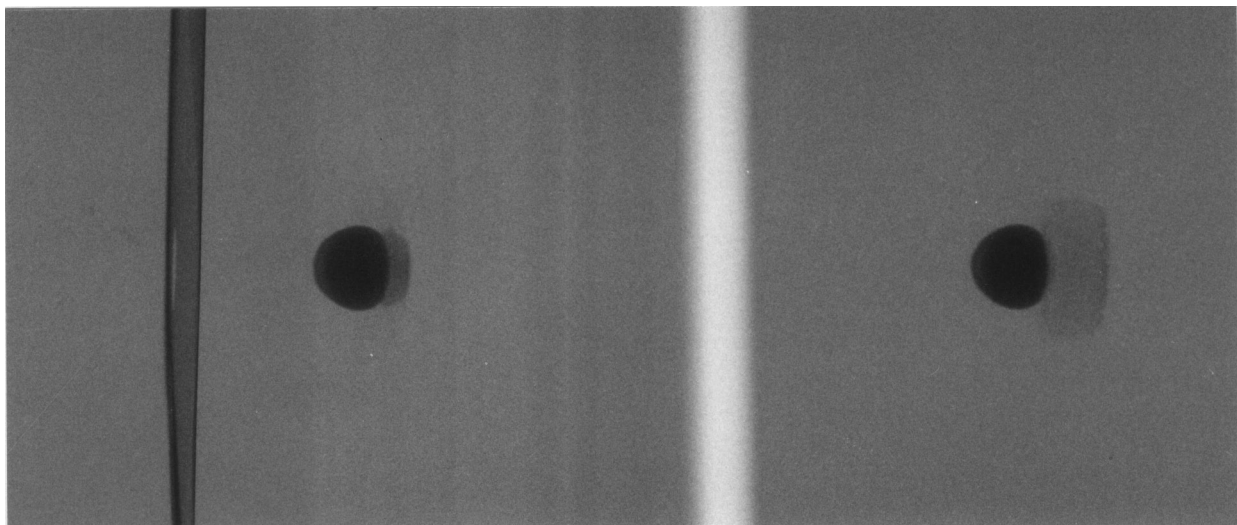

Fig. 6. Radiograph of the deformed sphere and the debris cloud produced by the impact of a 9.53-mm-diameter, 2017-T4 aluminum sphere with a 0.076-mm-thick, 1100-H18 aluminum sheet at 7.19 km/s (Shot 4-1910). The views were made 3.4 and 15.6 μs after impact.

Table 2. Normalized velocities of front element for higher velocity tests using 9.53-mm-diameter, 2017-T4 aluminum spheres as projectiles

Shot Number	Bumper Sheet Alloy	$\frac{t}{D}$	Impact Velocity, (km/s)	Normalized Axial Velocities		Normalized Diametral Velocities	
				V_1/V_0	V_2/V_0	V_{Front}/V_0	V_{Rear}/V_0
4-1910	1100-H18	0.008	7.19	1.046	0.997	0.083	0.074
4-1395	6061-T6	0.026	6.70	1.030	0.991	0.079	0.124
4-1290	1100-O	0.032	6.67	1.018	0.982	0.082	0.130
4-1360	6061-T6	0.049	6.62	1.012	0.980	0.084	0.137
4-1744	6061-T6	0.049	7.38	1.031	0.966	0.089	0.186
4-1282	2024-T3	0.053	6.58	1.002	0.962	0.088	0.152
4-1359	6061-T6	0.062	6.78	1.001	0.968	0.099	0.143
4-1289	6061-T6	0.084	6.68	0.986	0.960	0.102	0.141
4-1283	6061-T6	0.102	6.72	0.973	0.955	0.114	0.149

and does not provide reliable measurement data since the front element has not expanded significantly. One pair of flash radiographs was used to observe the spheres and debris clouds for Shots 4-1870 and 4-1874 and, as a result, these two tests could not provide velocity data. Qualitatively, the debris clouds produced by these two tests had the same form and characteristics as those shown for Shots 4-1897 and 4-1910.

In Table 2, V_1 and V_2 are the axial velocities of the leading edge of the front element and the deformed sphere, respectively. The normalized axial velocity of the front element, V_1/V_0, was *greater* than 1 until the t/D ratio was greater than 0.062, indicating that the post impact velocity of this feature was greater than the impact velocity. The normalized axial velocity of the deformed sphere, V_2/V_0, was *less* than 1 for all test conditions, indicating that the post impact velocity of the sphere was less than the impact velocity. In both cases, the normalized axial velocities decreased as the t/D ratio of the tests was increased. Both normalized axial velocities are shown as a function of t/D ratio in Fig. 7.

Also shown in Fig. 7 are the normalized diametral expansion velocities, V_{Front}/V_0 and V_{Rear}/V_0, of the front and rear of the front element, respectively. The normalized diametral expansion velocity of the leading edge, V_{Front}/V_0, remained relatively constant up to a t/D ratio of 0.049. The value of V_{Front}/V_0 increased slightly when the t/D ratio was greater than 0.049, but did not appear to be affected by changes in the impact velocity, at least within the limits imposed by the measurement techniques used to obtain these data. The other three normalized velocities given for Shot 4-1744, at 7.38 km/s, are noticeably more or less than the values shown for a second test with the same t/D ratio (Shot 4-1360) and an impact velocity that was in the velocity range of the majority of the tests listed in Table 2.

On the other hand, the normalized diametral expansion velocity, V_{Rear}/V_0, of the rear of the front element increased very quickly as the t/D ratio increased from 0.008. The normalized diametral velocity of the *rear* of the front element was greater than the normalized diametral velocity of the *leading edge* of the front element in all tests presented in Table 2, except for Shot 4-1910. Both normalized diametral velocities increased slightly with increasing t/D ratio when the t/D ratio was greater than 0.053. As shown in Ref. 1, these increases and an accompanying change in the shape of the front element were due to interactions with other parts of the evolving debris cloud.

The results of the four recent tests with the very thin bumper sheets indicate that the dark substructure of the front element, for the test shown in Fig. 5, was formed from a plug of bumper material and a portion of the front of the sphere that experienced quasi one-dimensional loading during the initial phase of impact. As shown in Fig 7, the normalized diametral velocity of the
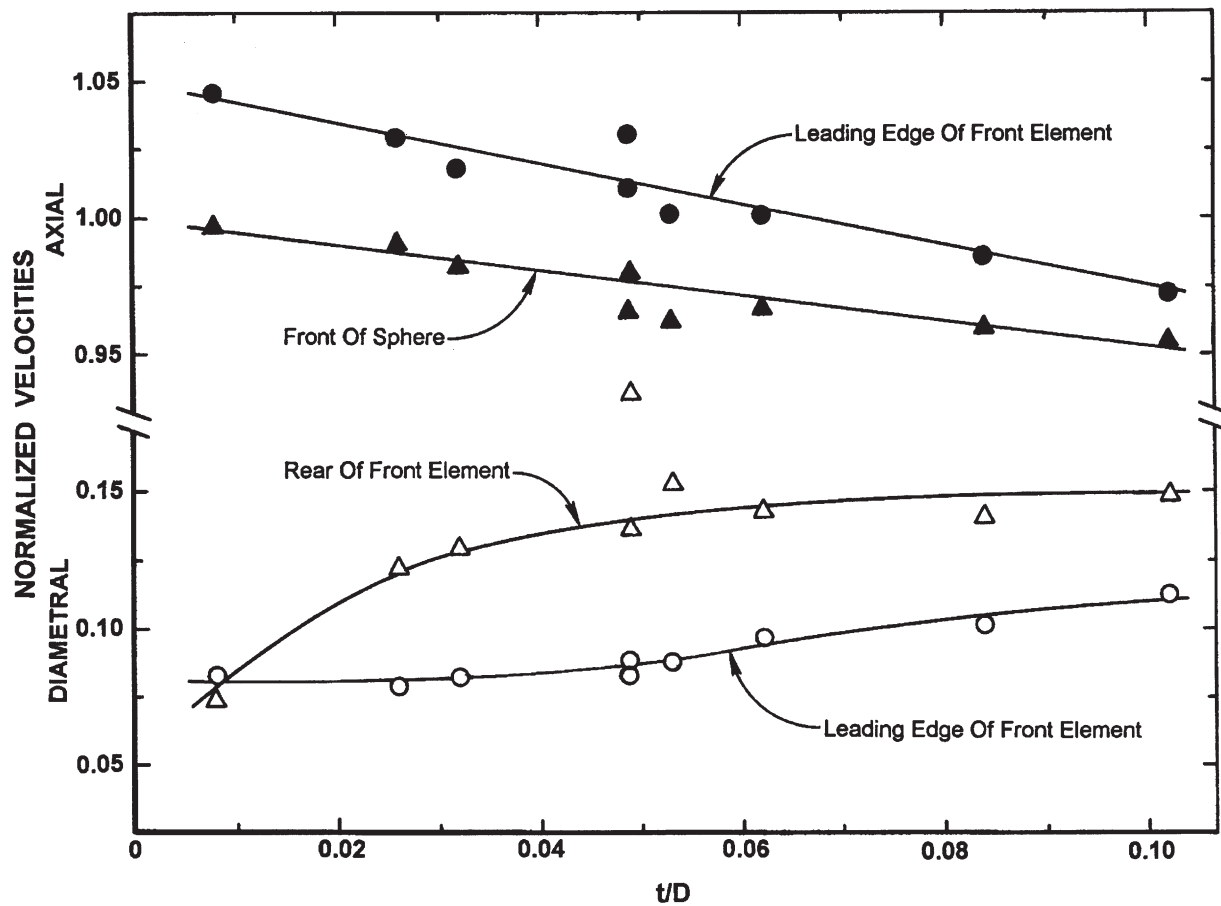
Fig. 7. Normalized axial and diametral velocities of the front element as a function of t/D ratio for tests using 9.53-mm-diameter, 2017-T4 aluminum spheres.

rear of the front element was less than the normalized diametral velocity of the leading edge of the front element for Shot 4-1910. The diameter of the leading edge of the front element for Shot 4-1910 was determined to be 45 percent of the diameter of the impacting sphere, less than is predicted (57 percent) by the model shown in Fig. 4. The rear of the *double* cross-hatched region in Fig. 5 corresponds to the rear of the front element observed for Shot 4-1910. The material that surrounded this region (shown with single cross hatches) was material from the bumper that began to experience some shock loading before the arrival of the sphere. In all of the tests shown in Table 2, with the exception of Shot 4-1910, the diametral velocity of the rear of the front element was taken to be the velocity of the diameter of the *single* cross-hatched region shown in Fig. 5. The front element and the substructure that were observed in the debris cloud for this test, Shot 4-1290, were also observed in the debris cloud for Shot 4-1395. They were not readily evident in the debris cloud for Shot 4-1360 or for tests with t/D ratios greater than 0.032.

The size and apparent density of the front element displayed in the radiographs of the tests with the very thin sheets was surprising. Frequently, it is assumed that very thin sheets (i.e., foil switches, printed-circuit velocity screens, etc.) placed a short distance in front of or on the front surface of targets used for hypervelocity impact experiments do not significantly affect the results of the tests. The results of the recent tests would indicate that the impact of a sphere with these thin sheets can seriously affect the integrity of the sphere. In addition, the debris generated by the impact of the projectile with the thin sheet can have a catastrophic effect on a target that is downrange of the thin sheet. In the tests with the thin bumper sheets, a 0.5-mm-thick, 2024-T3 aluminum witness plate was placed about 38 cm downrange of the bumpers. A view of the witness plate from Shot 4-1910 is shown in Fig. 8. The deformed sphere did not come in contact with the witness plate because a hole that was several times larger that the sphere was formed in
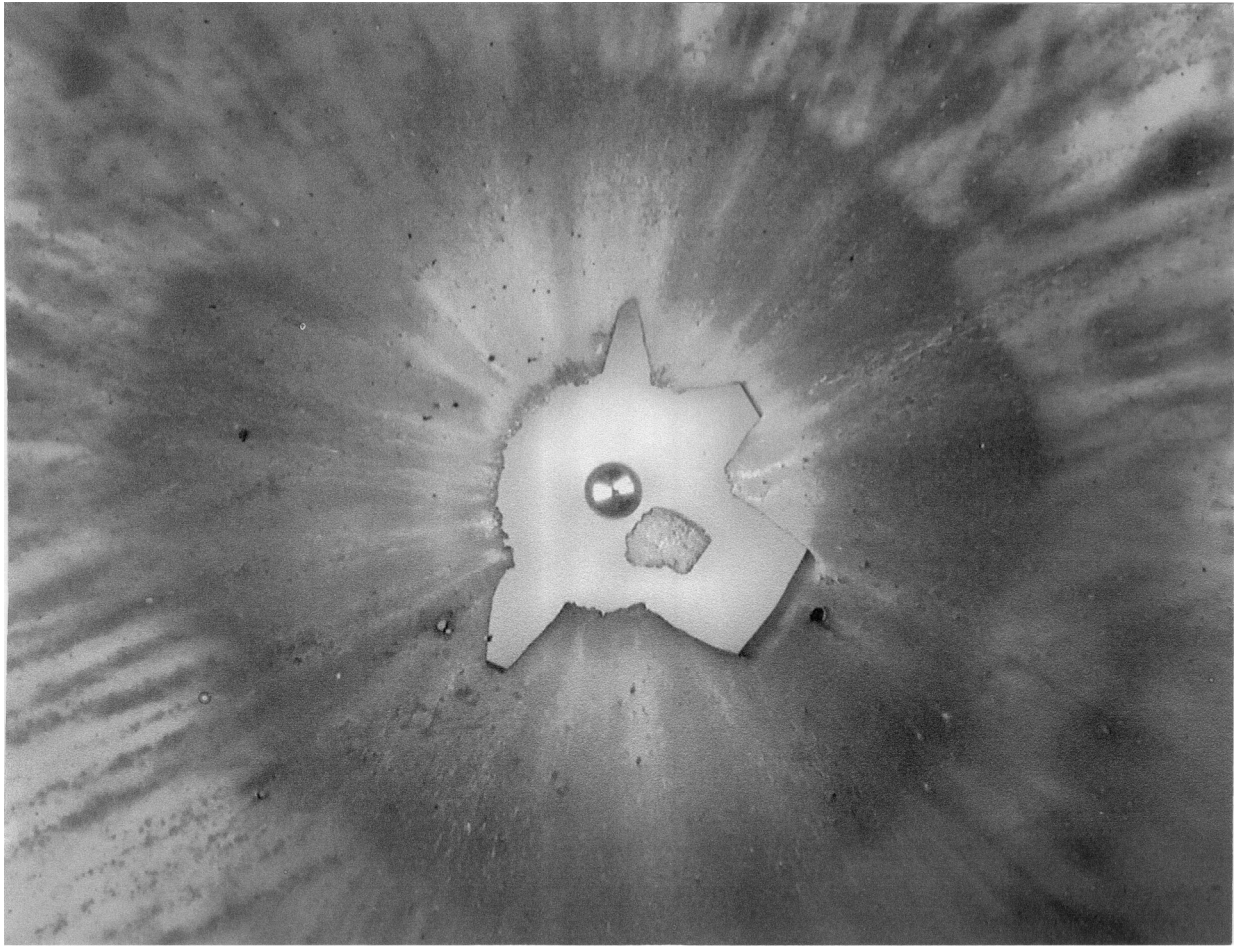
Fig. 8. View of the damage pattern produced on a 0.5-mm-thick, 2024-T3 aluminum witness plate by the debris cloud formed by the impact of a 9.53-mm-diameter, 2017-T4 aluminum sphere with a 0.076-mm-thick, 1100-H18 aluminum sheet at 7.19 km/s (Shot 4-1910). The witness plate was 38 cm downrange of the target sheet.

the witness plate by the front element before the arrival of the sphere. As was shown in Fig. 6, the diameter of the front element was greater than the diameter of the sphere when the debris cloud was less than 12 cm downrange. The region of the witness plate that was impacted by the front element was 3.7 cm in diameter and was covered with numerous small craters. The witness plate had a number of 0.2-mm- to 0.3-mm-diameter perforations scattered around the central part of the cratered region. The craters at the periphery of the cratered region were slightly deeper than those in the rest of the affected region. In addition, some of the peripheral craters exhibited pinhole-sized perforations. The perforations were irregularly spaced but were found around the entire periphery of the cratered region. The nearly instantaneous arrival of all of the droplets making up the front element applied a large impulsive load to the witness plate. This impulsive load, coupled with cratering effects, perforation, and heating produced by the impact of the very large number of droplets, caused the sheet to rupture and petal in the severely affected area. All of the petals shown in Fig. 8 had a portion of the cratered region attached to the tip of the petal. Several small cratered sections of the sheet were torn loose during the rupture process. One of the cratered pieces of the witness plate and a 9.53-mm-diameter aluminum sphere is shown in the hole produced by the impact of the front element of the debris cloud.

4. Conclusions

A relationship developed in earlier work was shown to accurately describe the fragmentation-initiation threshold velocity for aluminum spheres impacting thin aluminum bumper sheets at normal incidence as a function of t/D ratio. The new work described in this paper extended the verified usefulness of a simple relationship describing the fragmentation threshold velocity to impact velocities up to 7.2 km/s. This new work also showed that the relationship could be used to determine the fragmentation threshold velocity for any diameter sphere by using the t/D ratio as the scaling factor.

Results of an analysis of the radiographs from the tests were used, in conjunction with a model for the formation of the front element of a debris cloud, to confirm the source of material making up the core of the front element.

Acknowledgment

References

[1]   Piekutowski AJ. Formation and description of debris clouds produced by hypervelocity impact. NASA 1996 CR-4707.

[2]   Gilath I, Eliezer S, Bar-Noy T, Englman R, Jaeger Z. Material response at hypervelocity impact conditions using laser induced shock waves. *Int. J. Impact Engng.* 1993; **14**: 279-289.

[3]   Ang JA. Impact flash jet initiation phenomenology. *Int. J. Impact Engng.* 1990: **10**: 23-33.